
LATENT DIFFUSION MODEL FOR CONDITIONAL RESERVOIR FACIES GENERATION

Daesoo Lee

Norwegian University of Science and Technology

Oscar Ovanger

Norwegian University of Science and Technology

Jo Eidsvik

Norwegian University of Science and Technology

Erlend Aune

Norwegian University of Science and Technology
BI Norwegian Business School
Abelee

Jacob Skauvold

Norwegian Computing Center

Ragnar Hauge

Norwegian Computing Center

ABSTRACT

Creating accurate and geologically realistic reservoir facies based on limited measurements is crucial for field development and reservoir management, especially in the oil and gas sector. Traditional two-point geostatistics, while foundational, often struggle to capture complex geological patterns. Multi-point statistics offers more flexibility, but comes with its own challenges. With the rise of Generative Adversarial Networks (GANs) and their success in various fields, there has been a shift towards using them for facies generation. However, recent advances in the computer vision domain have shown the superiority of diffusion models over GANs. Motivated by this, a novel Latent Diffusion Model is proposed, which is specifically designed for conditional generation of reservoir facies. The proposed model produces high-fidelity facies realizations that rigorously preserve conditioning data. It significantly outperforms a GAN-based alternative. Our implementation on GitHub: <https://released-on-accept>.

Keywords Conditional facies generation · Reservoir facies · Diffusion model · Latent Diffusion Model

1 Introduction

Creating accurate and geologically realistic reservoir facies predictions based on limited measurements is a critical task in the oil and gas sector, specifically in field development and reservoir management. It is also very relevant in connection with CO₂ storage, where one makes decisions about injection strategies to manage leakage risk and ensure safe long-term operations. Key operational decisions are often based on realizations of stochastic reservoir models. Through the use of multiple realizations, one can go beyond point-wise prediction of facies, and additionally quantify spatial variability and correlation. This can give a better description, and hence a better understanding, of the relevant heterogeneity.

When generating facies realizations, one must honor both geological knowledge and reservoir-specific data. A wide range of stochastic models have been proposed to solve this problem. A good overview can be found in the book by Pyrcz and Deutsch (2014). There are variogram-based models, where the classical concept of a variogram-based Gaussian field (see for instance Cressie, 2015) is combined with a discretization scheme to generate facies. Then there are more geometric approaches, such as object models or process-mimicking models, where facies are described as geometric objects with an expected shape and uncertainty. Of particular interest here are multiple-point models, which use a training image to generate a pattern distribution, and then generate samples following this distribution.

Multiple-point models are very flexible, and allow for complex interactions between any number of facies. But as the method fundamentally hinges on storing pattern counts, there are strict limitations due to memory. In practice, only a limited number of patterns can be handled, leading to restrictions in pattern size and a demand for stationarity of patterns. Furthermore, the simulation algorithm has clear limitations in its ability to reproduce the patterns, so a realization will typically contain many patterns not found in the initial database, leading to unwanted geometries (Zhang et al., 2019). Limitations like these have led to the adoption of models such as generative adversarial networks (GANs, Goodfellow et al., 2020). In recent years, GANs have gained substantial attention for the conditional generation of realistic facies while retaining conditional data in a generated sample, see e.g. Chan and Elsheikh (2019); Zhang et al. (2019); Azevedo et al. (2020); Pan et al. (2021); Song et al. (2021); Zhang et al. (2021); Yang et al. (2022); Razak and Jafarpour (2022); Hu et al. (2023).

We frame stochastic facies modeling as a conditional generation problem in machine learning. This framing is motivated by the observation that in some existing methods for reservoir modeling, generating unconditional realizations is comparatively easy, and the difficulty increases sharply as one moves to generating conditional realizations. The principal idea of this paper is to exploit this difficulty gap by using easily generated unconditional realizations as training data for a machine learning model. Crucially, this model will learn not only how to reproduce features seen in the training realizations, but also how to honor conditioning data. A model successfully trained in this way can generate conditional realizations given previously unseen conditioning data. Fig. 1 illustrates our conditional generation problem.

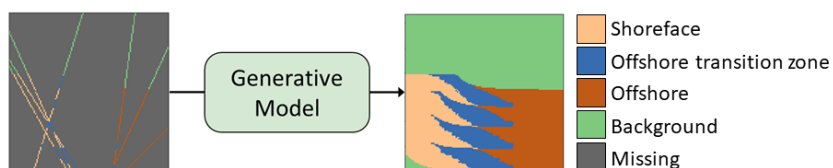


Figure 1: Illustration of our conditional reservoir generation problem in which the generative model stochastically samples a realistic reservoir (right) given the limited measurements (left). In our dataset, three different facies are present, colored in beige, blue, and brown, respectively, while the non-facies regions are marked in green. Additionally, the regions with no information are denoted in grey.

Recent studies in computer vision have demonstrated the superiority of diffusion models over GANs in terms of generative performance (Rombach et al., 2022; Dhariwal and Nichol, 2021; Ho et al., 2022; Kim et al., 2022). As a result, diffusion models are state-of-the-art for image generation, while the popularity of GANs has diminished due to limitations including convergence problems, mode collapse, generator-discriminator imbalance, and sensitivity to hyperparameter selection. Latent diffusion models (Rombach et al., 2022) are a type of diffusion model in which the diffusion process occurs in a latent space rather than in pixel space. LDMs have become popular because they combine computational efficiency with good generative performance.

Motivated by the progress made with diffusion models on computer vision and image processing tasks, this work proposes a novel LDM, specifically designed for the generation of conditional facies realizations in a reservoir modeling context. Its appeal lies in its ability to strictly preserve conditioning data in the generated realizations. To the authors' knowledge, this is the first work to adopt a diffusion model for conditional facies generation.

Experiments were carried out using a dataset of 5,000 synthetic 2D facies realizations to evaluate the proposed diffusion model against a GAN-based alternative. The diffusion model achieved robust conditional facies generation performance in terms of fidelity, sample diversity, and the preservation of conditional data, while a GAN-based model struggled with multiple critical weaknesses.

To summarize, the contributions of this paper are:

1. the adoption of a diffusion model for conditional facies generation,
2. a novel LDM, designed to preserve observed facies data in generated samples,
3. conditional facies generation with high fidelity, sample diversity, and robust preservation.

In Section 2, we describe GANs and background information for the LDMs. In Section 3, we present our suggested methodology for conditional facies realizations with LDMs. In Section 4, we show experimental results of our method applied to a bedset model with stacked facies, including the comparison with GANs. In Section 5, we summarize and discuss future work.

2 Background on Generative Models

2.1 Generative Adversarial Network for Conditional Image Generation

Generative Adversarial Network were a breakthrough innovation in the field of generative AI when they emerged in 2014. The core mechanism of GANs involves two neural networks, a generator and a discriminator, engaged in a sort of cat-and-mouse game. The generator aims to mimic the real data, while the discriminator tries to distinguish between real and generated data. Through iterative training, the generator improves its ability to create realistic data, and the discriminator becomes more adept at identifying fakes.

Conditional Generative Adversarial Networks (CGANs) were proposed by Mirza and Osindero (2014) in the same year as the GAN. The CGAN was designed to guide the image generation process of the generator given conditional data such as class labels and texts as auxiliary information. Since then, CGANs have been further developed to perform various tasks. Among these, Isola et al. (2017) stands out from the perspective of conditional facies generation, proposing a type of CGAN called Pixel2Pixel (Pix2Pix), which has become a popular GAN method for image-to-image translation. Pix2Pix works by training a CGAN to learn a mapping between input images and output images from different distributions. For instance, the input could be a line drawing, and the output a corresponding color image. The mapping can be realized effectively with the help of the U-Net architecture (Ronneberger et al., 2015), illustrated in Figure 2. Fig. 2 illustrates the U-Net architecture.

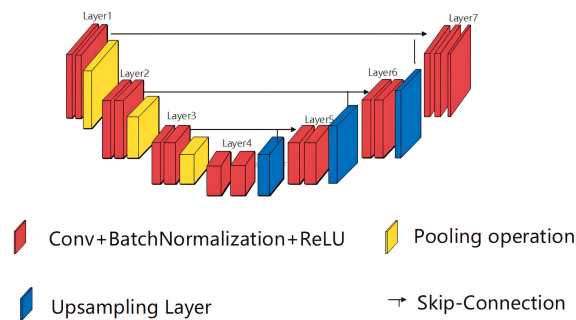


Figure 2: Illustration of the U-Net architecture (Cai et al., 2022), where Conv denotes a convolutional layer. U-Net is a convolutional neural network architecture, featuring an encoder (first half of U-Net) and decoder (second half) structure with skip connections that allow for the transfer of spatial information across layers, which in turn enables precise localization and high-resolution output.

Image-to-image translation is directly relevant to conditional facies generation because the input can be facies observations on a limited subset of the model domain, and the output can be a complete facies model. This is the typical situation when the goal is to generate 2D or 3D facies realizations from sparse facies observations at the well locations.

2.2 GANs for Conditional Facies Generation

Dupont et al. (2018) was the first work to adopt a GAN for conditional facies generation, overcoming the limitations of traditional geostatistical methods by producing varied and realistic geological patterns that honor measurements at data points. However, the latent vector search required to ensure a match with the conditioning data makes the sampling process inefficient. Chan and Elsheikh (2019) introduced a second inference network that enables the direct generation of realizations conditioned on observations, thus providing a more efficient conditional sampling approach. Zhang et al. (2019) introduced a GAN-based approach to generate 3D facies realizations, specifically focusing on complex fluvial and carbonate reservoirs. This paper also clearly demonstrated the superiority of GAN over MPS for this application. Azevedo et al. (2020) used GANs in a similar way, but the evaluation of its conditional generation makes this study different from others. Where GANs from other studies are typically conditioned on multiple sparse points, this paper considers conditioning on patches and lines. Because such shapes typically involve a larger region than multiple sparse points, their conditional setup is more difficult, which is demonstrated in their experiment. Pan et al. (2021) was the first work to use Pix2Pix, adopting the U-Net architecture. It takes a facies observation and noise as input, and then stochastically outputs a full facies realization. Notably, the preservation of conditional data in a generated sample was shown to be effective due to the U-Net architecture that enables precise localization. Zhang et al. (2021) is concurrent with and methodologically similar to Pan et al. (2021) as both articles propose a GAN built on U-Net. However, the U-Net GAN of Zhang et al. (2021) has an additional loss term to ensure sample diversity, which simplifies the sampling process. Subsequently, many studies have sought to improve conditional facies generation using GANs, working within

the same or similar frameworks as the studies mentioned above Song et al. (2021); Yang et al. (2022); Razak and Jafarpour (2022); Hu et al. (2023).

The main difference between this study and previous research is the type of generative model employed, specifically the choice of a diffusion model over a GAN. This also leads to a specific network architecture used to enable conditioning. Another difference is that whereas much earlier work is done in a top-down view, we focus on a vertical section. A consequence of this is that we get a different structure for the conditioning data. In a vertical section, well data become paths, giving connected lines of cells with known facies. In the top-down view, wells appear as scattered individual grid cells with known facies.

2.3 Denoising Diffusion Probabilistic Model (DDPM)

Ho et al. (2020) represented a milestone for diffusion model-based generative modeling. DDPMs offer a powerful framework for generating high-quality image samples from complex data distributions. At its core, a DDPM leverages the principles of diffusion processes to model a data distribution. It operates by iteratively denoising a noisy sample and gradually refining it to generate a realistic sample as illustrated in Fig. 3. This denoising process corresponds to the reverse process of a fixed Markov process of a certain length.

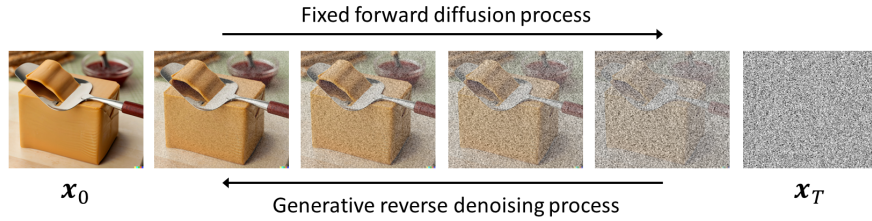


Figure 3: Illustration of the principle of a diffusion process. The diffusion modeling mainly consists of 1) forward process (noising) and 2) reverse process (denoising). The noising process begins with a data sample and incrementally adds Gaussian noise over multiple time steps to convert it into a Gaussian noise sample; conversely, the denoising process iteratively refines this Gaussian noise sample back into a data-like sample, guided by a neural network trained specifically for this denoising task.

A DDPM employs a denoising autoencoder, denoted by $\epsilon_{\theta}(\mathbf{x}_t, t); t = 1, \dots, T$. The denoising autoencoder gradually refines the initial noise \mathbf{x}_T to generate a high-quality sample \mathbf{x}_0 that closely resembles the target data distribution. A U-Net is used for the denoising autoencoder since its architecture provides effective feature extraction, preservation of spatial details, and robust performance in modeling complex data distributions (Baranchuk et al., 2021).

Training: Prediction of Noise in \mathbf{x}_t DDPM training consists of two key components: the non-parametric forward process and the parameterized reverse process. The former component represents the gradual addition of Gaussian noise. In contrast, the reverse process needs to be learned to predict noise ϵ in \mathbf{x}_t . Its loss function is defined by

$$L_{\text{DDPM}} = \mathbb{E}_{\mathbf{x}, \epsilon \sim \mathcal{N}(\mathbf{0}, \mathbf{I}), t} [\|\epsilon - \epsilon_{\theta}(\mathbf{x}_t, t)\|_2^2], \quad (1)$$

where ϵ_{θ} denotes the denoising autoencoder with parameters θ . Eq. (1) measures the discrepancy between the noise and the predicted noise by the denoising autoencoder. While Eq. (1) defines a loss function for unconditional generation, the loss for conditional generation is specified by

$$L_{\text{DDPM},c} = \mathbb{E}_{\mathbf{x}, c, \epsilon \sim \mathcal{N}(\mathbf{0}, \mathbf{I}), t} [\|\epsilon - \epsilon_{\theta}(\mathbf{x}_t, t, c)\|_2^2], \quad (2)$$

where c denotes conditional data such as texts or image class, and in our situation, the observed facies classes in wells. Typically, L_{DDPM} and $L_{\text{DDPM},c}$ are both minimized during training, to allow both unconditional and conditional generation. For details, see Ho and Salimans (2022).

Sampling via Learned Reverse Process The forward diffusion process is defined as $q(\mathbf{x}_t | \mathbf{x}_{t-1}) = \mathcal{N}(\mathbf{x}_t; \sqrt{1 - \beta_t} \mathbf{x}_{t-1}, \beta_t \mathbf{I})$ where β_t is called a variance schedule and $1 \geq \beta_T > \beta_1 \geq 0$. Equivalently, it can be written $\mathbf{x}_t = \sqrt{1 - \beta_t} \mathbf{x}_{t-1} + \sqrt{\beta_t} \epsilon_{t-1}$ with $\epsilon_{t-1} \sim \mathcal{N}(\mathbf{0}, \mathbf{I})$. We further reformulate the equation with respect to \mathbf{x}_{t-1} and it becomes

$$\begin{aligned} \mathbf{x}_{t-1} &= (\mathbf{x}_t - \sqrt{\beta_t} \epsilon_{t-1}) / \sqrt{1 - \beta_t} \\ &= (\mathbf{x}_t - \sqrt{1 - \alpha_t} \epsilon_{t-1}) / \sqrt{\alpha_t}, \end{aligned} \quad (3)$$

where $\alpha_t = 1 - \beta_t$. Then we can go backwards, sampling \mathbf{x}_0 from \mathbf{x}_T by recursively applying Eq. (3) for $t = T, \dots, 2, 1$.

2.4 Latent Diffusion Model (LDM)

LDMs extend DDPMs by introducing a diffusion process in a latent space. The main idea of LDMs is illustrated in Fig. 4, aligning with the overview of our proposed method for conditional facies generation as depicted in Fig. 5. In the common situation, data are typically text or images as indicated to the far right in Fig. 4. In our setting, the conditional data are facies observations along a few well paths in the subsurface.

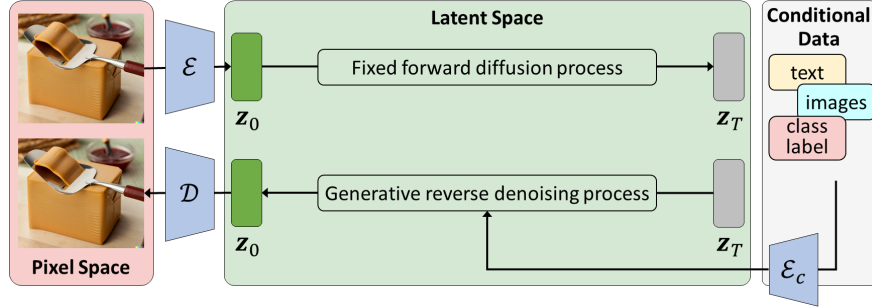


Figure 4: Overview of LDM. The encoder \mathcal{E} and decoder \mathcal{D} enable data compression, enabling the forward and reverse processes to operate in a reduced-dimensional space. This eases the task of learning prior and posterior distributions and improves computational efficiency. In addition, conditional data can be fed into the reverse process, enabling conditional generation.

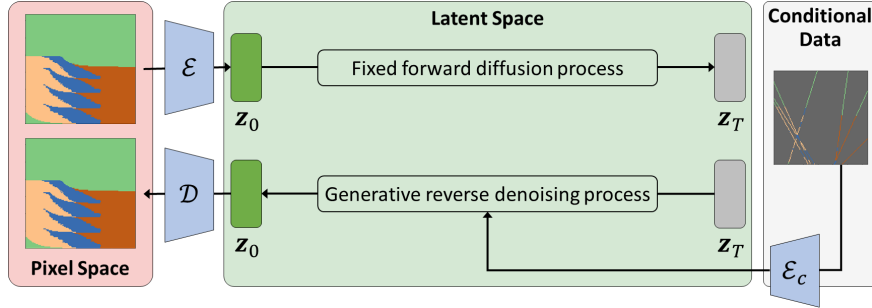


Figure 5: Overview of our proposed method. Our method can be regarded as an adapted version of LDM to effectively handle the categorical input and allow maximal preservation of conditional facies data in generated facies while maintaining the high fidelity of generated facies.

Compared with a DDPM, an LDM has two additional components: encoder \mathcal{E} and decoder \mathcal{D} . The encoder transforms \mathbf{x} into a latent representation, $\mathbf{z} = \mathbf{z}_0 = \mathcal{E}(\mathbf{x})$, while the decoder reconstructs \mathbf{z} to produce $\tilde{\mathbf{x}}$. Importantly, the encoding and decoding processes involve downsampling and upsampling operations, respectively. The encoder and decoder are trained so that $\tilde{\mathbf{x}}$ is as close as possible to \mathbf{x} . This is ensured by minimizing a reconstruction loss between \mathbf{x} and $\tilde{\mathbf{x}}$. Notably, the forward and backward processes are now taking place in the latent space, therefore \mathbf{z}_T denotes a Gaussian noise sample. In Fig. 4, \mathcal{E}_c denotes an encoder for conditional data. The encoded conditional data is fed into the reverse process for conditioning the generation process.

The main advantage of LDMs over DDPMs is computational efficiency. The encoder \mathcal{E} compresses high-dimensional data \mathbf{x} into a lower-dimensional latent space represented via latent variable \mathbf{z} . This dimensionality reduction significantly reduces the computational cost, making LDM more feasible to be trained on local devices. However, a trade-off exists between computational efficiency and sample quality. Increasing the downsampling rate of \mathcal{E} increases the computational efficiency but typically results in a loss of sample quality, and vice versa.

Training of LDMs adopts the two-staged modeling approach (Van Den Oord et al., 2017; Chang et al., 2022). The first stage (stage 1) is for learning the compression and decompression of \mathbf{x} by training \mathcal{E} and \mathcal{D} , and the second stage (stage 2) is for learning the prior and posterior distributions by training ϵ_θ .

In stage 1, \mathbf{x} is encoded into \mathbf{z} and decoded back into the data space. The training of \mathcal{E} and \mathcal{D} is conducted by minimizing the following reconstruction loss:

$$\|\mathbf{x} - \mathcal{D}(\mathcal{E}(\mathbf{x}))\|_2^2. \quad (4)$$

In stage 2, the denoising autoencoder ϵ_θ is trained to learn prior and posterior distributions by minimizing Eq. (5) and Eq. (6), respectively, while \mathcal{E} and \mathcal{D} are set to be untrainable (frozen).

$$L_{\text{LDM}} = \mathbb{E}_{\mathcal{E}(x), \epsilon \sim \mathcal{N}(\mathbf{0}, \mathbf{I}), t} [\|\epsilon - \epsilon_\theta(\mathbf{z}_t, t)\|_2^2], \quad (5)$$

$$L_{\text{LDM},c} = \mathbb{E}_{\mathcal{E}(x), c, \epsilon \sim \mathcal{N}(\mathbf{0}, \mathbf{I}), t} [\|\epsilon - \epsilon_\theta(\mathbf{z}_t, t, c)\|_2^2]. \quad (6)$$

The recent work that proposed DALLE-2 (Ramesh et al., 2022) empirically found that predicting \mathbf{z}_0 instead of ϵ results in better training. We adopt the same approach for better training and methodological simplicity of our conditional sampling. Hence, we in stage 2 instead minimize

$$L_{\text{LDM}}(\mathbf{z}, g_\theta) = \mathbb{E}_{\mathcal{E}(x), \epsilon \sim \mathcal{N}(\mathbf{0}, \mathbf{I}), t} [\|\mathbf{z}_0 - g_\theta(\mathbf{z}_t, t)\|_2^2], \quad (7)$$

$$L_{\text{LDM},c}(\mathbf{z}, c, g_\theta) = \mathbb{E}_{\mathcal{E}(x), c, \epsilon \sim \mathcal{N}(\mathbf{0}, \mathbf{I}), t} [\|\mathbf{z}_0 - g_\theta(\mathbf{z}_t, t, c)\|_2^2], \quad (8)$$

where g_θ is a denoising autoencoder that predicts \mathbf{z}_0 instead of ϵ . Then sampling in the latent space can be formulated as $q(\mathbf{z}_{t-1} | \mathbf{z}_t, \mathbf{z}_0) = \mathcal{N}(\mathbf{z}_{t-1}; \tilde{\mu}_t(\mathbf{z}_t, \mathbf{z}_0), \tilde{\beta}_t \mathbf{I})$ where $\tilde{\mu}_t(\mathbf{z}_t, \mathbf{z}_0) = \frac{\sqrt{\alpha_t - 1} \beta_t}{1 - \bar{\alpha}_t} \mathbf{z}_0 + \frac{\sqrt{\alpha_t} (1 - \bar{\alpha}_{t-1})}{1 - \bar{\alpha}_t} \mathbf{z}_t$, $\tilde{\beta}_t = \frac{1 - \bar{\alpha}_{t-1}}{1 - \bar{\alpha}_t} \beta_t$, and $\bar{\alpha}_t = \prod_{s=1}^t \alpha_s$. Equivalently, we have

$$\mathbf{z}_{t-1} = \tilde{\mu}_t(\mathbf{z}_t, \mathbf{z}_0) + \sqrt{\tilde{\beta}_t} \epsilon. \quad (9)$$

Then we can sample \mathbf{z}_0 from \mathbf{z}_T by recursively applying

$$\mathbf{z}_{t-1} = \tilde{\mu}_t(\mathbf{z}_t, g_\theta(\mathbf{z}_t, t)) + \sqrt{\tilde{\beta}_t} \epsilon. \quad (10)$$

3 Methodology

We here propose our LDM method tailored for conditional reservoir facies generation with maximal preservation of conditional data. We first describe the differences between image generation and reservoir facies generation that are important to be considered in the design of our method, and then outline the proposed method.

3.1 Differences between Image Generation and Reservoir Facies Generation

There are several distinct differences between the image generation problem and the reservoir facies generation problem that pose challenges in employing an LDM for reservoir facies generation:

Input Types In image generation, an input image is considered continuous and one has $\mathbf{x} \in \mathbb{R}^{3 \times H \times W}$ where 3, H , and W denote RGB channels, height, and width, respectively. In the reservoir facies generation, however, the input is categorical $\mathbf{x} \in \mathbb{Z}_2^{F \times H \times W}$ where $\mathbb{Z}_2 \in \{0, 1\}$, F denotes the number of facies types, and each pixel, denoted by $\mathbf{x}_{:hw} = \mathbf{x}_{fhw} \forall f = 1, 2, \dots, F$, is a one-hot-encoded vector where 1 for a corresponding facies type index, 0 otherwise. The conditional data of \mathbf{x} , notated as \mathbf{x}_c has a dimension of $(F + 1 \times H \times W)$. It has one more dimension than \mathbf{x} for indicating a masked region.

Properties of Conditional Data The domains of conditional data in LDM are often different from the target domain. It can for instance be a text prompt, which is among the most common conditional domains. In the conditional reservoir facies generation, unlike common applications of LDMs, the conditional domain corresponds to the target domain. Importantly, its conditional data \mathbf{x}_c is spatially aligned with \mathbf{x} .

Strict Requirement to Preserve Conditional Data in Generated Sample In an LDM, the conditioning process has cross-attention (Vaswani et al., 2017) between the intermediate representations of the U-Net and the representation of conditional data obtained with \mathcal{E}_c . One way of viewing this is that the encoded conditional data is mapped to the U-Net as auxiliary information. However, an LDM has a caveat in the conditional generation – that is, its conditioning mechanism is not explicit but rather implicit. To be more specific, conditional data is provided to the denoising autoencoder, but the denoising process is not penalized for insufficiently honoring the conditional data. As a result, LDMs are often unable to fully preserve conditional data in the generated sample but rather only capture the context of conditional data. The limitation has been somewhat alleviated using classifier-free guidance (Ho and Salimans, 2022), but the problem still persists. Our problem with facies generation requires precise and strict preservation of conditional data in the generated data. In other words, facies measurements in wells should be retained in the predicted facies realization. Therefore, an explicit conditioning mechanism needs to be incorporated.

3.2 Proposed Method

Our proposed method, tailored for conditional reservoir facies generation, is based on LDMs, leveraging its computational efficiency and resulting feasibility. The suggested method addresses several key aspects, including proper handling of the categorical input type, effective mapping of conditional data to the generative model, and maximal preservation of conditional data through a dedicated loss term for data preservation. Fig. 6 presents the overview of the training process of our proposed method.

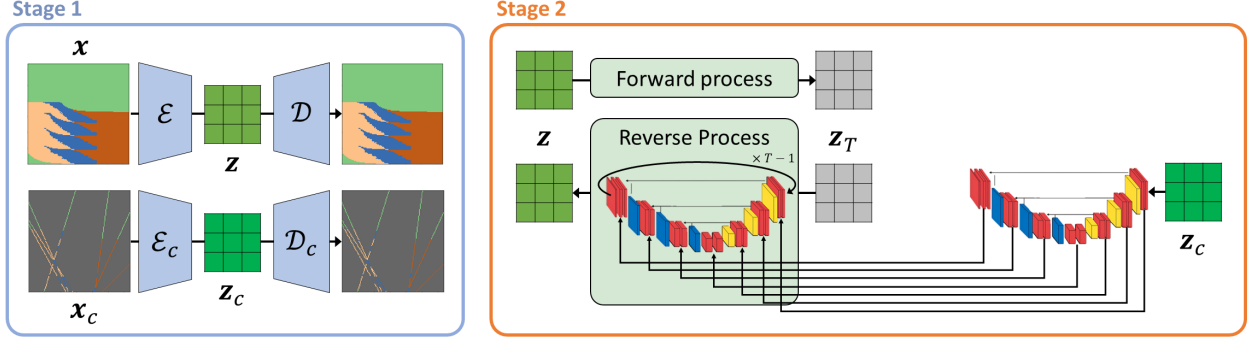


Figure 6: Overview of the training process of our proposed method. It consists of two subsequent training stages: stage 1 for learning to compress and decompress data, and stage 2 for learning the conditional denoising process. Two U-Nets are used in stage 2. One is for the denoising process and the other is for extracting the intermediate representations of z_c . After completing the training process, the generation of a new sample (sampling process) involves the denoising of z_T into $z_0 = z$, using Eq. (10), followed by its decoding into the data space, which is expressed as $\mathcal{D}(z)$.

Stage 1 has two pairs of encoder and decoder, trained to compress and decompress \mathbf{x} and \mathbf{x}_c , respectively. The first pair is \mathcal{E} and \mathcal{D} for the unconditional part, and the second pair is \mathcal{E}_c and \mathcal{D}_c for the conditional part. Here, \mathcal{E} compresses \mathbf{x} to \mathbf{z} , while \mathcal{E}_c compresses \mathbf{x}_c to \mathbf{z}_c . Because \mathbf{x} and \mathbf{x}_c are spatially aligned, we use the same architectures for \mathcal{E} and \mathcal{E}_c , and \mathcal{D} and \mathcal{D}_c . Furthermore, our input is categorical as $\mathbf{x} \in \mathbb{Z}_2^{F \times H \times W}$ and $\mathbf{x}_c \in \mathbb{Z}_2^{F+1 \times H \times W}$. Therefore, we cannot naively use the stage 1 loss of LDM in Eq. (4). We tackle the limitation by reformulating the task as a classification task instead of a regression. Hence, our loss function in stage 1 is based on the cross-entropy loss function and it is formulated as:

$$L_{\text{stage1}} = \mathbb{E}_{\mathbf{x}, h, w} \left[- \sum_f \mathbf{x}_{fhw} \log \text{softmax}(\mathcal{D}(\mathcal{E}(\mathbf{x}))_{fhw}) - \sum_f (\mathbf{x}_c)_{fhw} \log \text{softmax}(\mathcal{D}_c(\mathcal{E}_c(\mathbf{x}_c))_{fhw}) \right] \quad (11a)$$

$$= \mathbb{E}_{\mathbf{x}, h, w} \left[- \sum_f \mathbf{x}_{fhw} \log \tilde{\mathbf{x}}_{fhw} - \sum_f (\mathbf{x}_c)_{fhw} \log (\tilde{\mathbf{x}}_c)_{fhw} \right] \quad (11b)$$

$$= CE(\mathbf{x}, \tilde{\mathbf{x}}) + CE(\mathbf{x}_c, \tilde{\mathbf{x}}_c) \quad (11c)$$

$$= L_{\text{recons}}(\mathbf{x}, \mathcal{E}, \mathcal{D}) + L_{\text{recons}}(\mathbf{x}_c, \mathcal{E}_c, \mathcal{D}_c), \quad (11d)$$

where CE denotes a cross-entropy loss function and L_{recons} denotes a reconstruction loss function.

Stage 2 is dedicated to learning prior and posterior distributions via learning the reverse denoising process. The learning process involves two important perspectives: 1) effective mapping of \mathbf{z}_c to the denoising autoencoder g_θ to enable the conditional generation and 2) maximal preservation of conditional data in the generated data.

To achieve the effective mapping of \mathbf{z}_c to g_θ , we employ two U-Nets with the same architecture to process \mathbf{z} and \mathbf{z}_c , respectively. The first U-Net is the denoising autoencoder g_θ and the second U-Net is denoted g_ϕ for extracting multi-level intermediate representations of \mathbf{z}_c . In the conditional denoising process, the intermediate representations of \mathbf{z}_c are mapped onto those of \mathbf{z}_t obtained with g_θ . This multi-level mapping enables a more effective conveyance of \mathbf{z}_c which in turn results in better preservation of conditional data in the generated facies realizations. The multi-level mapping is possible because \mathbf{x} and \mathbf{x}_c are spatially aligned, and equivalently for \mathbf{z} and \mathbf{z}_c with their intermediate representations from the U-Nets.

To achieve maximal preservation of conditional data, we explicitly tell the generative model to preserve \mathbf{x}_c in the generated sample by introducing the following loss:

$$L_{\text{preserv}} = CE(\mathbf{x}_c, \hat{\mathbf{x}}_c), \quad (12)$$

where $\hat{\mathbf{x}}_c$ represents a softmax prediction of \mathbf{x}_c and is a subset of $\hat{\mathbf{x}}$ in which $\hat{\mathbf{x}} = \text{softmax}(\mathcal{D}(\hat{\mathbf{z}}))$ and $\hat{\mathbf{z}} \sim p_{\theta}(\mathbf{z}|\mathbf{z}_t, g_{\phi}(\mathbf{z}_c))$. Here, $p_{\theta}(\mathbf{z}|\mathbf{z}_t, g_{\phi}(\mathbf{z}_c))$ denotes the conditional probabilistic generative denoising process to sample $\hat{\mathbf{z}}$, given \mathbf{z}_t and $g_{\phi}(\mathbf{z}_c)$.

The backpropagation of L_{preserv} , however, encounters a bottleneck problem in the conventional setting of stage 2 where an encoder and decoder are set to be untrainable (frozen). This backpropagation traverses through \mathcal{D} , extending to both g_{θ} and g_{ϕ} , and therefore \mathcal{D} emerges as a problem when the parameters of \mathcal{D} are fixed. To remove the bottleneck, we set \mathcal{D} to be trainable, while \mathcal{E} is still set to be untrainable (frozen) in stage 2.

Finally, our loss function in stage 2 is defined by

$$L_{\text{stage2}} = \{p_{\text{uncond}}L_{\text{LDM}}(\mathbf{z}, g_{\theta}) + (1 - p_{\text{uncond}})L_{\text{LDM},c}(\mathbf{z}, g_{\phi}(\mathbf{z}_c), g_{\theta})\} + L_{\text{preserv}}, \quad (13)$$

where p_{uncond} is a constant probability of unconditional generation, typically assigned a value of either 0.1 or 0.2 (Ho and Salimans, 2022).

4 Experiments

Our dataset comprises 5,000 synthetic reservoir facies samples, partitioned into training (80%) and test datasets (20%). For details about the geological modeling assumptions about bedset stacking and facies sampling, see Appendix A. In our experiments, we assess the effectiveness of our proposed version of an LDM for both conditional and unconditional facies generation. Furthermore, we present a comprehensive comparative analysis of our diffusion model against a GAN-based approach. Specifically, we adopt the U-Net GAN from Zhang et al. (2021) due to its similar conditional setup to ours and showed good performance in terms of fidelity and sample diversity in the conditional generation of binary facies. For the details of our diffusion model and U-Net GAN, see Appendix B and Appendix C, respectively.

4.1 Conditional Facies Generation by the Proposed Diffusion Model

In the sampling process, the denoising autoencoder iteratively performs denoising to transition \mathbf{z}_T (Gaussian noise) into \mathbf{z}_0 with each step being conditioned on the encoded conditional data. To provide a granular insight into the progressive denoising process, we present a visual example of transitions of the conditional denoising process in Fig. 7. (Additional examples are presented in Fig. 14 in Appendix E.) At the beginning of the denoising process ($t = 1000 = T$), \mathbf{z}_t is initially composed of random Gaussian noises. Consequently, $\mathcal{D}(\mathbf{z}_t)$ also represents noise, resulting in a significant preservation error. However, as the denoising steps progress towards $t = 0$, the generated facies gradually becomes more distinct and recognizable while the preservation error becomes smaller.

In Fig. 7, \mathbf{x}_c is sourced from the test dataset, and we visualize the most probable facies types within $\mathcal{D}(\mathbf{z}_t)$. It is important to emphasize that $\mathcal{D}(\mathbf{z}_t)$ belongs to the space $\mathbb{Z}_2^{F \times H \times W}$, where the most probable facies type corresponds to the channel f with the highest value. The results demonstrate the effectiveness of the denoising process of our method. We notice the gradual improvement in the fidelity of the generated facies and the preservation error, eventually producing realistic facies that honor the conditional data.

The denoising process is stochastic, therefore various facies can be generated given \mathbf{x}_c . In Fig. 8, multiple instances of conditionally-generated facies are showcased for different \mathbf{x}_c . Each row in this display hence represents multiple realizations of facies models, given the well facies data (second column of each row).

The results highlight the efficacy of our diffusion model in capturing the posterior and sample diversity while adhering to given constraints. In particular, the conditional generation can be notably challenging, especially when there is a substantial amount of conditional data to consider (*e.g.*, the third row in Fig. 8). However, our diffusion model demonstrates its capability to honor the conditional data while generating realistic facies faithfully. This capability facilitates the quantification of uncertainty associated with the generated facies, providing valuable insights for decision-makers in making informed decisions. With the bedset model, the well data contain much information about the transition zone from one facies type to another. This information clearly constrains the variability in the conditional samples, and there is not so much variability within the samples in a single row compared with the variability resulting from different well configurations and facies observations in the wells.

The sample diversity stands in contrast to other approaches such as GANs, which frequently encounter a mode collapse problem, resulting in a considerable reduction in sample diversity. This deficiency often necessitates the incorporation of an additional loss term to partially mitigate the problem (Zhang et al., 2021).

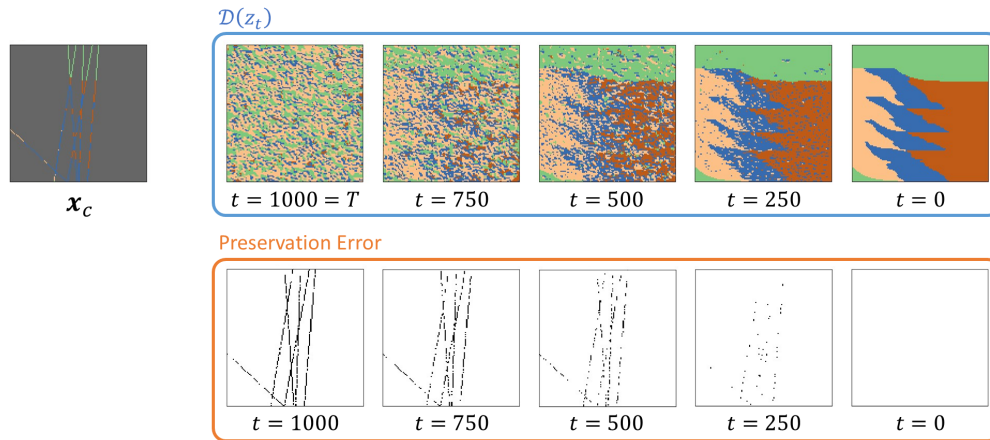


Figure 7: Visualization of transitions in the conditional denoising process. The denoising autoencoder sequentially denoises z_T to z_0 , conditioned on the encoded x_c , in the sampling process. Each z_t in the process can be decoded and visualized to gain a better understanding of the conditional denoising process. We present $\mathcal{D}(z_t)$ at the denoising steps of 1000, 750, 500, 250, and 0, where $T = 1000$ in this setup. The preservation error indicates the degree of accuracy with which the conditional data is retained within the generated data. Pixels colored in black indicate the error.

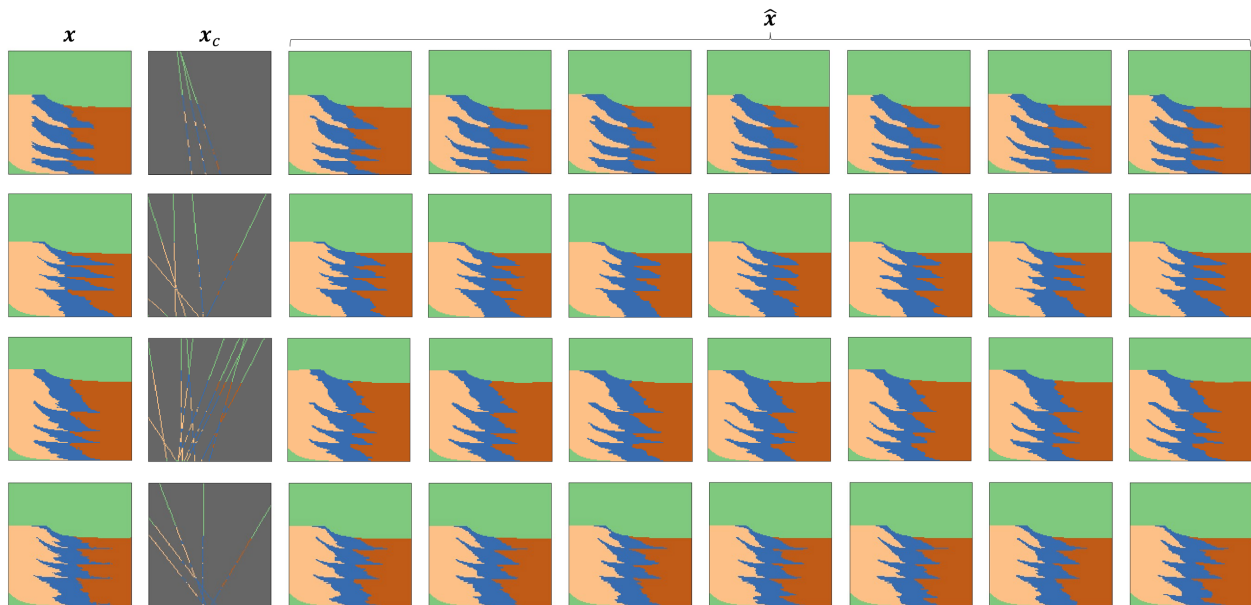


Figure 8: Examples of multiple instances of generated facies conditioned on different x_c using our diffusion model. The first and second columns represent x (ground truth) and x_c , respectively, from the test dataset, and the rest of the columns represent the conditionally generated facies with the preservation error maps. It is important to emphasize that the preservation error maps are omitted here because a preservation error rarely occurs.

4.2 Conditional Facies Generation by GAN and Its Limitations

We next show results of using a GAN on this reservoir facies generation problem. As commonly observed in the GAN literature, we experienced a high level of instability in training with a U-Net GAN. Fig. 9 presents the training history of the U-Net GAN. First, the gap between the generator and discriminator losses becomes larger as the training progresses. This indicates that it suffers from the generator-discriminator imbalance problem. Second, the discriminator loss eventually converges, while the generator loss diverges towards the end of the training. This exhibits the divergent loss problem and results in a complete failure of the generator. Third, the loss for preserving x_c is unstable and non-convergent due to the unstable training process of the GAN. Lastly, the sample diversity loss indicates better

diversity when the loss value is lower and vice versa. Throughout the training process, the diversity loss remains high until shortly before 9000 epochs, then the generator fails and starts producing random images. The failure leads to a decrease in the diversity loss. It indicates that the GAN model struggles to capture a sample diversity while retaining good generative performance.

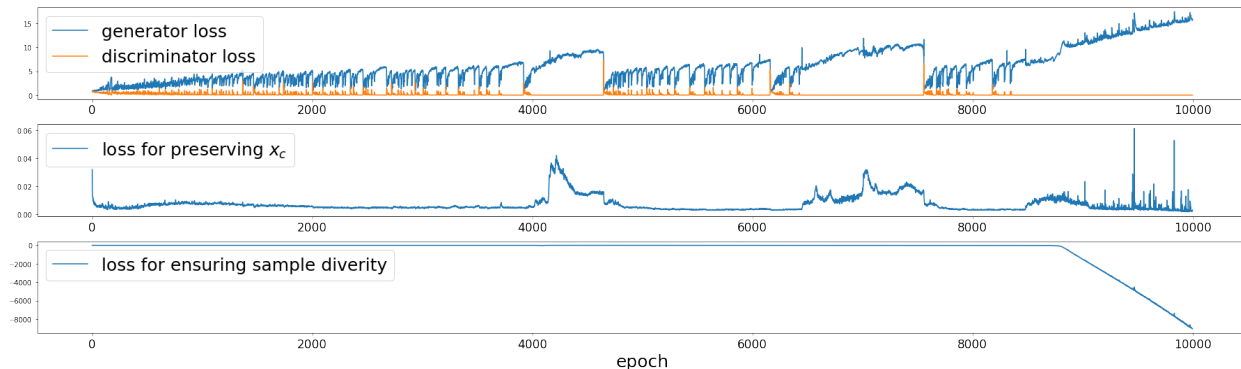


Figure 9: Training loss history of U-Net GAN. The training process exhibits issues such as non-convergence, imbalance between the generator and discriminator, and divergent loss.

Fig. 10 shows conditionally-generated samples using U-Net GAN at different training steps. The unstable training process can be seen in the generated samples. For instance, we observe a noticeable improvement in the quality of generated facies up to the 3000 training epoch. However, at the 4000 epoch, there is an abrupt decline in the quality. Subsequently, there is a partial recovery across the 5000 and 6000 epochs. Nevertheless, the quality significantly drops at the 7000 epoch, and by the time the epoch reaches 9000, the generated samples are barely recognizable. Generally, the GAN model appears to face challenges in concurrently maintaining high fidelity, preserving conditional data, and achieving sample diversity, therefore failing to capture the posterior.

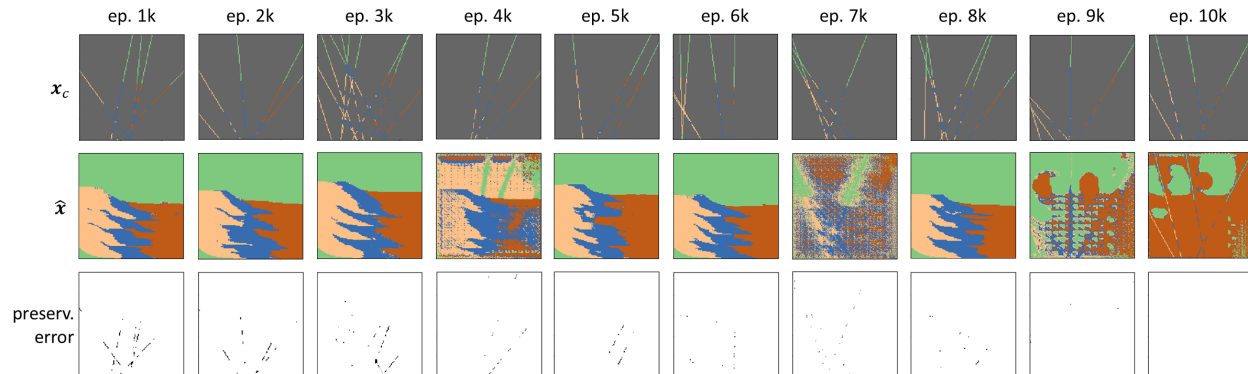


Figure 10: Visualization of conditionally-generated facies samples by U-Net GAN at different training steps with the preservation error map. ep. denotes epoch, and x and x_c are from the test dataset.

Fig. 11 presents multiple instances of generated facies conditioned on different x_c using the U-Net GAN. The generator at the training epoch of 8000 is used to generate the samples for its better performance than the generators at the other epochs. The results show that the generated samples have low fidelity, considerable deviations from the ground truths, and a lack of sample diversity due to the mode collapse. Furthermore, the generated samples exhibit a large sum of preservation errors, indicating the incapability to retain the conditional data. Overall, the results demonstrate that the GAN model fails to capture the posterior.

Table 1 specifies the preservation error rates of our proposed diffusion model and the U-Net GAN. The preservation error rate is defined as

$$\text{Preservation error rate} = \frac{\text{a number of different pixels between } x_c \text{ and } \text{argmax } \hat{x}_c \text{ for the valid pixels in } x_c}{\text{a number of valid pixels in } x_c},$$

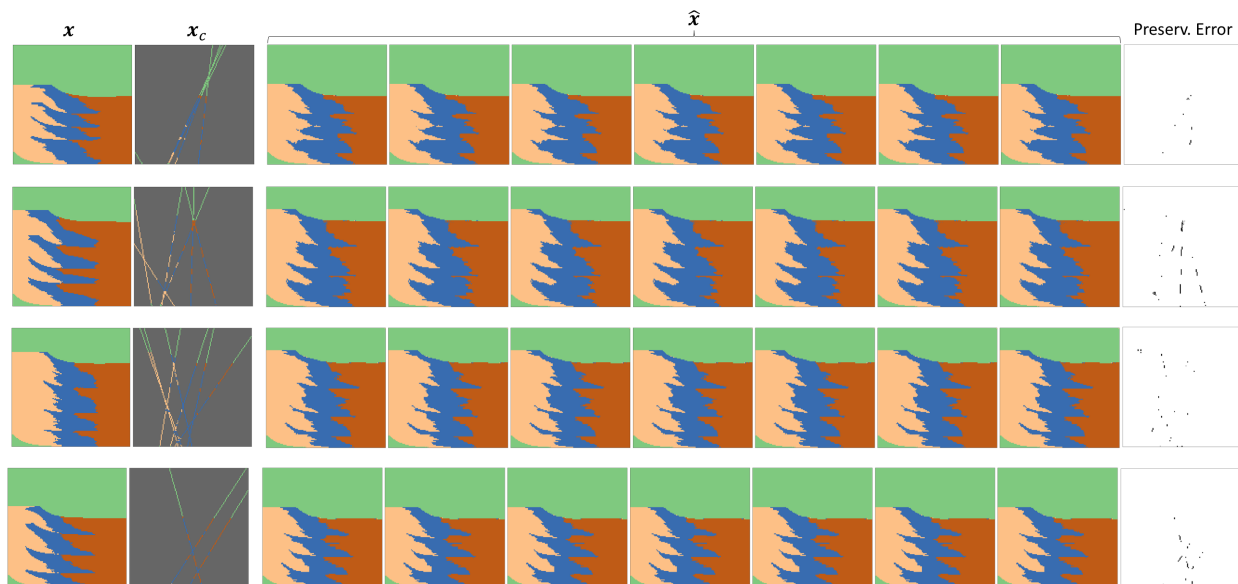


Figure 11: Examples of multiple instances of generated facies conditioned on different x_c using U-Net GAN. The first and second columns represent x (ground truth) and x_c , respectively, from the test dataset, \hat{x} denotes the conditionally generated facies, and the last column shows the preservation error maps. It is important to highlight that we are showcasing a total of seven distinct generated samples. Nevertheless, they appear to be identical, primarily as a result of the mode collapse phenomenon that occurs during the GAN training. Because the generated facies are identical, their corresponding preservation error maps are also identical. Hence, we present a single preservation error map on the right-hand side.

where the preservation error rate of zero indicates perfect preservation. The results demonstrate that our diffusion model achieves the near-perfect preservation (*i.e.*, only 0.03% of conditional data fails to be retained) and it significantly outperforms the U-Net GAN in retaining conditional data, surpassing it by a factor of approximately 200 times.

Table 1: Preservation error rates of our diffusion model and U-Net GAN on the test dataset.

	Our Diffusion Model	U-Net GAN
Preservation error rate	0.0003	0.05831

To better illustrate the mode collapse phenomenon in U-Net GANs in comparison to our proposed diffusion model, Fig. 12 shows a comparison between the prior distributions of the training and test datasets along with the prior distribution predicted by our diffusion model and that of the U-Net GAN. To visualize the prior distributions of the training and test datasets, we first employ an argmax operation on x across the channel dimension. This operation results in $\text{argmax} x \in \mathbb{R}^{H \times W}$ that contains integer values. Subsequently, we calculate the average of $\text{argmax} x$ for all instances of x within the training or test dataset. The same visualization procedure is applied to visualize the prior distributions predicted by our diffusion model and U-Net GAN, with the only difference being the application of an argmax operation to generated facies data. For the U-Net GAN, its generator at the 8000 training epochs is used (same as above). The prior distribution shows four main distinct colors (dark teal, light teal, yellow, and purple), and between the different facies, there exist intermediate areas where different facies can occur, represented by the intermediate colors. These results clearly demonstrate our diffusion model’s capability to accurately capture the prior distribution, whereas the U-Net GAN faces substantial challenges in this regard due to the mode collapse, leading to severe underestimation of the variability in the generated samples.

In the bottom displays of Fig. 12, we show the Jensen-Shannon (JS) divergence of the generated samples compared with the true model. Similar to the Kullback-Leibler divergence, but non-symmetric and finite (between 0 and 1), the JS divergence here measures the probabilistic difference between the generated and training samples. Clearly, the divergence is much smaller for the LDM here, while the GAN gets very large JS divergence (close to 1) at some of the facies boundaries. Even though it is less prominent than for the GAN, the divergence for LDM shows some structure near the facies transition zones. This indicates some underestimation in the implicit posterior sampling variability.

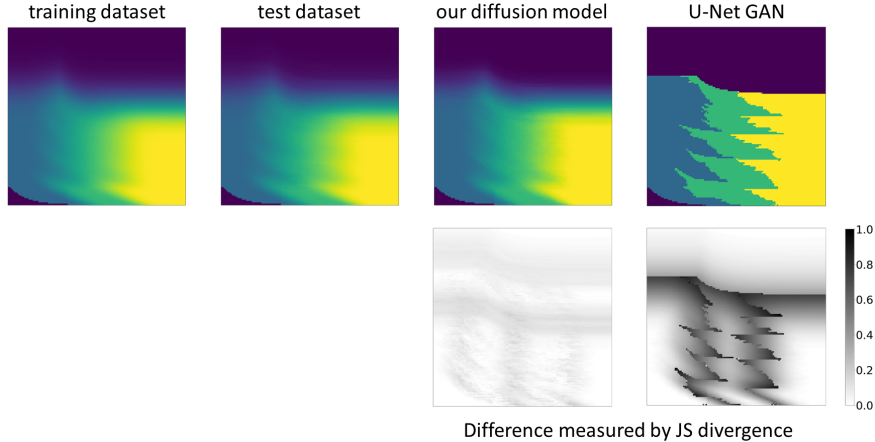


Figure 12: Comparative visualization of the prior distributions of the training and test datasets and the prior distribution predicted by our diffusion model and the U-Net GAN. The binary-colored figure depicts the discrepancy, measured by JS divergence, between the prior distribution of the training dataset and the predicted prior distribution. At every pixel, there exists a prior distribution encompassing various facies types, where these facies types are visually represented by distinct colors. The presence of intermediate colors signifies a prior distribution with greater diversity. In this context, it is important to highlight that the mode collapse observed in the U-Net GAN results in a reduction of sample diversity, analogous to the absence of those intermediate colors in the visualization.

4.3 Ablation Study

We conduct an ablation study to investigate the effects of the use of the proposed components such as L_{preserv} , trainable \mathcal{D} in stage2, and the multi-level mapping of z_c . The evaluation is performed on the test dataset. Table 2 outlines the specific Case (a)-(d) considered in the ablation study, and Table 3 reports L_{LDM} from Eq. (7), $L_{\text{LDM},c}$ from Eq. (8), L_{recons} from Eq. (11d), L_{preserv} , and a preservation error rate.

When analyzing these results, several key findings emerge. Firstly, in Case (b), both L_{preserv} and the preservation error rate exhibit a significant increase compared to Case (a). This increase can be attributed to the fact that the denoising model in (b) was not explicitly trained to preserve the conditional data, resulting in a notable degradation in preservation quality. Moving on to Case (c), we observe slightly elevated values for both L_{LDM} and $L_{\text{LDM},c}$. This outcome can be explained by the challenges posed during training due to the ineffective backpropagation of L_{preserv} , caused by the presence of the untrainable \mathcal{D} which also hinders the preservation ability. Case (d) sheds light on the effectiveness of the multi-level mapping, comparing L_{preserv} and the preservation error rate from the baseline Case (a). It emphasizes the positive impact of the multi-level mapping approach on preservation. Overall, the ablation study reveals that each component in our methodology plays a vital role in enhancing the overall preservation capacity of the conditional sampling.

Table 2: Ablation study cases with respect to the novel and essential components in stage 2. The signs of o and x indicate the use of the item described in the corresponding column name, where o and x denote using and not using, respectively. In the case of (d), instead of employing multi-level mapping for z_c , it takes a straightforward route to integrate x_c into the denoising U-Net. This integration is achieved through a simple concatenation of z_c and z_t , forming the input denoted as $[z_t, z_c]$ for the denoising U-Net, where $[\cdot]$ represents the concatenation operation.

	L_{preserv}	Trainable \mathcal{D}	Multi-level mapping of z_c
(a) Base	o	o	o
(b) – L_{preserv}	x	o	o
(c) – Trainable \mathcal{D}	o	x	o
(d) – Multi-level mapping of z_c	o	o	x

Table 3: Effects of the use of L_{preserv} , trainable \mathcal{D} , and multi-level mapping of z_c for the ablation study cases.

	(a) Base	(b) – L_{preserv}	(c) – Trainable \mathcal{D}	(d) – Multi-level mapping of z_c
L_{LDM}	0.0236	0.0226	0.0438	0.0262
$L_{\text{LDM},c}$	0.0238	0.0224	0.0437	0.0263
L_{recons}	0.0028	0.0042	0.0031	0.0046
L_{preserv}	0.0006	0.0111	0.001	0.0025
Preservation error rate	0.0003	0.0094	0.011	0.0017

5 Conclusion

We have introduced a novel approach for conditional reservoir facies modeling employing LDM. Experimental results show exceptional abilities to preserve conditional data within generated samples while producing high-fidelity samples. Our novelties lie in the proposals to enhance the preservation capabilities of LDM. Throughout our experiments, we have demonstrated the robustness and superiority of our diffusion-based method when compared to a GAN-based approach, across multiple aspects including fidelity, sample diversity, and conditional data preservation. Furthermore, we have presented the critical limitations of the GAN approach, which result in compromised fidelity, limited sample diversity, and sub-optimal preservation performance.

Overall, our work opens up a new avenue for conditional facies modeling through the utilization of a diffusion model. The results indicate some underestimation in the posterior samples, which can possibly improved by more nuanced training or refined loss functions. As future work, we aim to study the statistical properties of the LDM in detail on various geostatistical models and extend our method for 3D facies modeling.

Expanding our method for 3D facies modeling may appear straightforward by merely substituting 2D convolutional layers with their 3D counterparts. However, dealing with 3D spatial data presents inherent complexities stemming from its high-dimensional nature. This can manifest in various challenges, including high computational demands and the difficult learning of prior and posterior distributions. Therefore, it may need to employ techniques like hierarchical modeling. This can involve employing a compact latent dimension size for sampling, followed by an upscaling mechanism similar to super-resolution, in order to enhance the feasibility and effectiveness of the 3D modeling.

Acknowledgements

We would like to thank the Norwegian Research Council for funding the Machine Learning for Irregular Time Series (ML4ITS) project (312062), the GEOPARD project (319951) and the SFI Centre for Geophysical Forecasting (309960).

Ethical Statement

No conflicts of interest were present during the research process.

References

- Azevedo, L., Paneiro, G., Santos, A., and Soares, A. (2020). Generative adversarial network as a stochastic subsurface model reconstruction. *Computational Geosciences*, 24(4):1673–1692.
- Baranchuk, D., Rubachev, I., Voynov, A., Khulkov, V., and Babenko, A. (2021). Label-efficient semantic segmentation with diffusion models. *arXiv preprint arXiv:2112.03126*.
- Cai, S., Wu, Y., and Chen, G. (2022). A novel elastomeric unet for medical image segmentation. *Frontiers in Aging Neuroscience*, 14:841297.
- Chan, S. and Elsheikh, A. H. (2019). Parametric generation of conditional geological realizations using generative neural networks. *Computational Geosciences*, 23:925–952.
- Chang, H., Zhang, H., Jiang, L., Liu, C., and Freeman, W. T. (2022). Maskgit: Masked generative image transformer. In *Proceedings of the IEEE/CVF Conference on Computer Vision and Pattern Recognition*, pages 11315–11325.
- Cressie, N. (2015). *Statistics for spatial data*. John Wiley & Sons.
- Dhariwal, P. and Nichol, A. (2021). Diffusion models beat gans on image synthesis. *Advances in neural information processing systems*, 34:8780–8794.

- Dosovitskiy, A., Beyer, L., Kolesnikov, A., Weissenborn, D., Zhai, X., Unterthiner, T., Dehghani, M., Minderer, M., Heigold, G., Gelly, S., et al. (2020). An image is worth 16x16 words: Transformers for image recognition at scale. *arXiv preprint arXiv:2010.11929*.
- Dupont, E., Zhang, T., Tilke, P., Liang, L., and Bailey, W. (2018). Generating realistic geology conditioned on physical measurements with generative adversarial networks. *arXiv preprint arXiv:1802.03065*.
- Genton, M. G. (2002). Classes of kernels for machine learning: A statistics perspective. *J. Mach. Learn. Res.*, 2:299–312.
- Goodfellow, I., Pouget-Abadie, J., Mirza, M., Xu, B., Warde-Farley, D., Ozair, S., Courville, A., and Bengio, Y. (2020). Generative adversarial networks. *Communications of the ACM*, 63(11):139–144.
- Ho, J., Jain, A., and Abbeel, P. (2020). Denoising diffusion probabilistic models. *Advances in neural information processing systems*, 33:6840–6851.
- Ho, J., Saharia, C., Chan, W., Fleet, D. J., Norouzi, M., and Salimans, T. (2022). Cascaded diffusion models for high fidelity image generation. *The Journal of Machine Learning Research*, 23(1):2249–2281.
- Ho, J. and Salimans, T. (2022). Classifier-free diffusion guidance. *arXiv preprint arXiv:2207.12598*.
- Hu, F., Wu, C., Shang, J., Yan, Y., Wang, L., and Zhang, H. (2023). Multi-condition controlled sedimentary facies modeling based on generative adversarial network. *Computers & Geosciences*, 171:105290.
- Isla, M. F., Schwarz, E., and Veiga, G. D. (2018). Bedset characterization within a wave-dominated shallow-marine succession: An evolutionary model related to sediment imbalances. *Sedimentary Geology*, 374:36–52.
- Isola, P., Zhu, J.-Y., Zhou, T., and Efros, A. A. (2017). Image-to-image translation with conditional adversarial networks. In *Proceedings of the IEEE conference on computer vision and pattern recognition*, pages 1125–1134.
- Kim, G., Kwon, T., and Ye, J. C. (2022). Diffusionclip: Text-guided diffusion models for robust image manipulation. In *Proceedings of the IEEE/CVF Conference on Computer Vision and Pattern Recognition*, pages 2426–2435.
- Kingma, D. P. and Ba, J. (2014). Adam: A method for stochastic optimization. *arXiv preprint arXiv:1412.6980*.
- Lee, D., Aune, E., and Malacarne, S. (2023a). Masked generative modeling with enhanced sampling scheme. *arXiv preprint arXiv:2309.07945*.
- Lee, D., Malacarne, S., and Aune, E. (2023b). Vector quantized time series generation with a bidirectional prior model. In *International Conference on Artificial Intelligence and Statistics*, pages 7665–7693. PMLR.
- lucidrains (2022). lucidrains/denoising-diffusion-pytorch. <https://github.com/lucidrains/denoising-diffusion-pytorch>.
- Mirza, M. and Osindero, S. (2014). Conditional generative adversarial nets. *arXiv preprint arXiv:1411.1784*.
- nadavbh12, Huang, Y.-H., Huang, K., and Fernández, P. (2021). nadavbh12/VQ-VAE. <https://github.com/nadavbh12/VQ-VAE>.
- Pan, W., Torres-Verdín, C., and Pyrcz, M. J. (2021). Stochastic pix2pix: a new machine learning method for geophysical and well conditioning of rule-based channel reservoir models. *Natural Resources Research*, 30:1319–1345.
- Pyrcz, M. J. and Deutsch, C. V. (2014). *Geostatistical reservoir modeling*. Oxford University Press, USA.
- Ramesh, A., Dhariwal, P., Nichol, A., Chu, C., and Chen, M. (2022). Hierarchical text-conditional image generation with clip latents. *arXiv preprint arXiv:2204.06125*, 1(2):3.
- Razak, S. M. and Jafarpour, B. (2022). Conditioning generative adversarial networks on nonlinear data for subsurface flow model calibration and uncertainty quantification. *Computational Geosciences*, 26(1):29–52.
- Rombach, R., Blattmann, A., Lorenz, D., Esser, P., and Ommer, B. (2022). High-resolution image synthesis with latent diffusion models. In *Proceedings of the IEEE/CVF conference on computer vision and pattern recognition*, pages 10684–10695.
- Ronneberger, O., Fischer, P., and Brox, T. (2015). U-net: Convolutional networks for biomedical image segmentation. In *Medical Image Computing and Computer-Assisted Intervention—MICCAI 2015: 18th International Conference, Munich, Germany, October 5-9, 2015, Proceedings, Part III 18*, pages 234–241. Springer.
- Song, S., Mukerji, T., and Hou, J. (2021). Gansim: Conditional facies simulation using an improved progressive growing of generative adversarial networks (gans). *Mathematical Geosciences*, pages 1–32.
- Van Den Oord, A., Vinyals, O., et al. (2017). Neural discrete representation learning. *Advances in neural information processing systems*, 30.
- Vaswani, A., Shazeer, N., Parmar, N., Uszkoreit, J., Jones, L., Gomez, A. N., Kaiser, Ł., and Polosukhin, I. (2017). Attention is all you need. *Advances in neural information processing systems*, 30.

- Yang, Z., Chen, Q., Cui, Z., Liu, G., Dong, S., and Tian, Y. (2022). Automatic reconstruction method of 3d geological models based on deep convolutional generative adversarial networks. *Computational Geosciences*, 26(5):1135–1150.
- Zhang, C., Song, X., and Azevedo, L. (2021). U-net generative adversarial network for subsurface facies modeling. *Computational Geosciences*, 25:553–573.
- Zhang, T.-F., Tilke, P., Dupont, E., Zhu, L.-C., Liang, L., and Bailey, W. (2019). Generating geologically realistic 3d reservoir facies models using deep learning of sedimentary architecture with generative adversarial networks. *Petroleum Science*, 16:541–549.

A Dataset

As test setting for our model, we have used a 2D vertical slice through a shoreface environment, with a facies transition from shoreface through offshore transition zone to offshore. We model objects at the bedset-scale, as this is an appropriate representation for understanding reservoir facies which is often used (Isla et al., 2018). Bedsets have a sequential nature, in which there is first phase with an influx of sediments and then a phase of hiatus, called a flooding event. Following this flooding surface which defined a separating bedset geometry, the next bedset is formed, and so on. A packet of bedsets is called a parasequence. We form 2D models of a single parasequence in this paper. Two essential features of the bedset surface is the amount of progression (progradation) and elevation (aggradation) of the shoreline. The amount of aggradation is controlled by the influx of sediments in the deposition phase, and the amount of progradation is controlled by the sea-level and the volume of sediment input.

The data in this study is generated by sampling the top surfaces of bedset objects as Gaussian random fields (GRFs) and filling the grid cells between bedset objects with facies values represented by integer values sampled from truncated Gaussian random fields (TGRFs), with a trend for facies defined by the top surface of the bedset. The following list includes all steps of the process-based generative process:

1. Initial Parameter Setup:

- Define initial parameters that will govern the behavior of the synthetic model.
 - m : The number of bedset objects.
 - τ : Truncation levels.
 - η_{M_1} : Matérn covariance parameter values that govern the behavior of the top surface.
 - η_{M_2} : Matérn covariance parameter values that determine the characteristics of the TGRF.
 - μ_{ap} : Mean values for aggradation and progradation parameters.
 - Σ_{ap} : Covariance matrix for aggradation and progradation.

2. Establish Initial Bathymetry:

- Define $\mathbf{h}_0(\mathbf{s}) = \exp(-\frac{\mathbf{s}}{10})$ to represent the depth of the bottommost bedset. This initial state gives a starting point for subsequent layers. \mathbf{s} represents grid nodes on the lateral axis.

3. Begin Repetition Loop:

- Repeat the next steps (4-9) m times to create the sequence of bedsets.

4. Sampling Progradation and Aggradation Parameters:

- For each bedset $i = 1, \dots, m$, sample values for progradation (p_i) and aggradation (a_i) from a normal distribution with means and covariances specified by μ_{ap} and Σ_{ap} .

5. Determining Mean Top Surface:

- Compute the mean elevation of the current bedset using: $\mu_{z_i} = \min\{1 + a_i, a_i + \exp(-\frac{\mathbf{s}-p_i}{10})\}$. This is the expected elevation for the bedset's top surface.

6. Sampling Top Surface:

- Sample bedset geometry elevations from a normal distribution: $\mathbf{h}_i \sim N(\mu_{\mathbf{h}_i}, \Sigma_{\mathbf{h}_i}(\eta_{M_1}))$, where η_{M_1} represents covariance structure parameters.

7. Setting the Shoreline:

- Modify \mathbf{h}_i such that values to the left of the progradation point are adjusted to the aggradation value:

$$\mathbf{h}_i = \begin{cases} 1 + a_i, & \text{if } \mathbf{s} < p_i \\ \mathbf{h}_i, & \text{else} \end{cases}. \text{ This ensures the shoreline is correctly set.}$$

8. Generating Bedset Facies Realization:

- Sample a 2D Truncated Gaussian Random Field (TGRF) for the current bedset facies: $\mathbf{f}_i \sim \text{TGRF}(\mu_f, \Sigma_f(\eta_{M_2}); \tau)$, where $\tau = (\tau_1, \tau_2)$ are truncation levels. The mean function is set to: $\mu_f(s_1, s_2) = -10s_1 - 3s_2$, where s_1 are values on the first axis and s_2 values on the second axis. The mean value is computed for $\mathbf{s}_1 = \mathbf{s}_2 = [1, 2, \dots, 128]$. The values of the realizations will then be:

$$\mathbf{f}_i = \begin{cases} 0, & \text{if } f_{i,s_1,s_2} < \tau_1 \\ 1, & \text{if } f_{i,s_1,s_2} > \tau_1 \text{ and } f_{s_1,s_2} < \tau_2 \\ 2, & \text{if } f_{i,s_1,s_2} > \tau_2 \end{cases}$$

9. Downsampling for Bedset Fitting:

- Adjust the generated TGRF realization so that it fits between the current top bedset separating surface \mathbf{h}_i and the previous one \mathbf{h}_{i-1} . This is done column-wise to fit the level of the current top surface at each grid point s_1 on the first axis. This ensures that the bedset facies realization matches the domain of the geological bedset structure.

10. Matrix Population:

- Populate the 128x128 realization matrix \mathbf{x} which is the combination of all the facies \mathbf{f} variables within all bedset geometries \mathbf{h} . The grid cells that are not within the parasequence are set to the value -1 .

The parameter values used for this experiment are listed in Table 4 The η parameters represent Matérn covariance

Table 4: Parameter values used in the facies modeling building on bedsets.

Parameter	Value
m	4
τ	[-4.5,-7.5]
η_{M_1}	[10,1,0.002]
μ_{ap}	[2.0,3.0]
Σ_{ap}	[[0.01,-0.001],[-0.001,0.1]]
η_{M_2}	[1/4,3/4,1/2]

inputs; the correlation length scale, smoothness scale and standard-deviation (Genton (2002)).

Figure 13 shows an illustration of the bedsets top surfaces (left) and the combined facies realization (right).

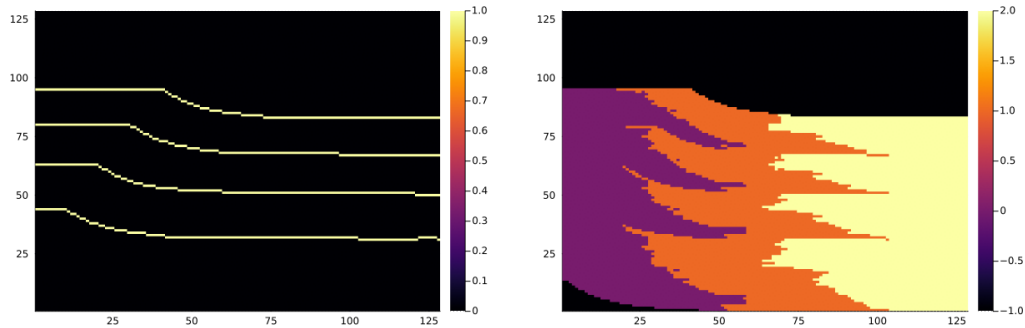


Figure 13: Realization of the top surfaces of a parasequence (left) and the corresponding facies variable (right).

The different facies represent different categories, therefore the facies data is represented in a one-hot encoding format, as described in Sect. 3.1. The conditional data \mathbf{x}_c is generated by taking a subset of \mathbf{x} with a random number of straight lines and random angles within certain ranges. The number of lines is sampled from $\text{Pois}(\lambda) + 1$ with λ of 4, where Pois denotes a Poisson distribution.

Our dataset comprises 5000 facies realizations, which we subsequently divided into training (80%) and test datasets (20%). The dataset is publicly available on https://figshare.com/articles/dataset/Geological_reservoir_facies_dataset/24235936.

B Implementation Details of Our Proposed Method

B.1 Encoders and Decoders: \mathcal{E} , \mathcal{E}_c , \mathcal{D} , and \mathcal{D}_c

The same encoder and decoder architectures from the VQ-VAE paper are used and their implementations are from nadavbh12 et al. (2021). The encoder consists of n downsampling convolutional blocks (Conv2d – BatchNorm2d – LeakyReLU), followed by m residual blocks (LeakyReLU – Conv2d – BatchNorm2d – LeakyReLU – Conv2d). The short notations are taken from the PyTorch implementations. The decoder similarly has m residual blocks, followed by n upsampling convolutional blocks. The upsampling convolutional layers are implemented with transposed convolutional layers (ConvTranspose2d). The hidden dimensions of the encoders and decoders are set to 64, and the bottleneck dimension (*i.e.*, dimension of \mathbf{z} and \mathbf{z}_c) is set to a small value like 4, following Rombach et al. (2022).

n determines a downsampling or compression rate, and we set it to 2. We did not use a high compression rate because a high value of n often leads to the loss of input information, resulting in an inadequate reconstruction of \mathbf{x}_c . This inadequacy suggests that \mathbf{z}_c fails to fully capture the information contained in \mathbf{x}_c , ultimately leading to a deficiency in preserving \mathbf{x}_c within a generated sample. In addition, Rombach et al. (2022) demonstrated that a low compression rate is sufficient for LDM to generate high-fidelity samples. As for m , we set it to 4.

In the naive form of \mathcal{E} and \mathcal{E}_c , the value ranges of \mathbf{z} and \mathbf{z}_c are not constrained. However, the diffusion model g_θ is designed to receive a value ranging between -1 and 1 (lucidrains, 2022). For instance, image data is scaled to range between -1 and 1 to be used as the input. To make \mathbf{z} and \mathbf{z}_c compatible with the diffusion model, we normalize them as $\mathbf{z}/\max(|\mathbf{z}|)$ and $\mathbf{z}_c/\max(|\mathbf{z}_c|)$, respectively.

Furthermore, we enhance the model by incorporating learnable positional embeddings, as demonstrated in Dosovitskiy et al. (2020), which are added to both \mathbf{z} and \mathbf{z}_c through concatenation. This addition is motivated by the presence of specific positional patterns within the facies data, and these learnable positional embeddings have the capability to capture and leverage such structures, introducing an inductive bias that helps the model generalize better to the typical positions of facies. The effectiveness of this approach was demonstrated in Dosovitskiy et al. (2020).

Lastly, our LDM adopts *VQ-reg* for \mathcal{D} and \mathcal{D}_c (Rombach et al., 2022). VQ-reg denotes that a vector quantization layer (Van Den Oord et al., 2017) is included in the decoder. To be more specific, the decoding process involves quantizing \mathbf{z} first and decoding it to \mathbf{x} .

B.2 U-Net

Two U-Nets are used in our proposed method – one for g_θ and the other for processing \mathbf{z}_c . The two U-Nets have the same architecture to have the same spatial dimensions for the multi-level mapping. We use the implementation of U-Net from lucidrains (2022). Its default parameter settings are used in our experiments except for the input channel size and hidden dimension size. To be more precise, we use `in_channels` (input channel size) of 4 because it is the dimension sizes of \mathbf{z} and \mathbf{z}_c AND `dim` (hidden dimension size) of 64.

B.3 Latent Diffusion Model

LDM is basically a combination of the encoders, decoders, and DDPM, where DDPM is present in the latent space. We use the implementation of DDPM from lucidrains (2022). Its default parameter settings are used in our experiments except for the input size and denoising objective for which we use the prediction of \mathbf{z}_0 instead of ϵ , as described in Sect. 2.4.

B.4 Optimizer

We employ the Adam optimizer (Kingma and Ba, 2014). We configure batch sizes of 64 and 16 for stage 1 and stage 2, respectively. The training periods are 200 epochs for stage 1 and 14000 steps (about 45 epochs) for stage 2.

B.5 Unconditional Sampling

The conditional sampling is straightforward as illustrated in Fig. 6. For the unconditional sampling, we replace \mathbf{z}_c with mask tokens, typically denoted as [MASK] or [M] (Lee et al., 2023b,a). The role of the mask token is to indicate that the sampling process is unconditional. The mask token is a learnable vector trained in stage 2 by minimizing $L_{\text{LDM}}(\mathbf{z}, g_\theta)$ in L_{stage2} .

C Implementation Details of U-Net GAN

We implement U-Net GAN, following the approach outlined in its original paper (Zhang et al., 2021). Two key hyperparameters govern the weighting of loss terms in this implementation: one for preserving conditional data (content loss) and the other for ensuring sample diversity (diverse loss). We maintain the same weights as specified in the paper, with a value of 0.05 for the diverse loss and 100 for the content loss. For optimization, we employ the Adam optimizer with a batch size of 32, a maximum of 10,000 epochs, and a learning rate set to 0.0002. The implementation is included in our GitHub repository.

D Pseudocode

To increase the reproducibility of our work and understanding of our codes in our GitHub repository, we present a pseudocode of the training process of our method in Algorithm 1 for stage 1 and Algorithm 2 for stage 2. In the pseudocodes, we provide a more detailed specification of \mathcal{D} . From a technical standpoint, \mathcal{D} is combined with VQ and denoted as \mathcal{D} with VQ-reg. This process entails the application of VQ initially, resulting in a discrete latent vector \mathbf{z} , which is subsequently processed by \mathcal{D} .

In Algorithm 1, ℓ_{VQ} and ℓ_{VQ_c} correspond to loss terms from VQ designed to minimize the disparity between \mathbf{z} and \mathbf{z}_q as introduced in the second and third terms of Equation (3) in Van Den Oord et al. (2017). The VQ losses, following the notations in Rombach et al. (2022), are omitted in the main section where VQ is integrated into \mathcal{D} .

Algorithm 1 Pseudocode of the training process of the proposed diffusion model (stage 1)

```

randomly initialize  $\mathcal{E}, \mathcal{E}_c, VQ, VQ_c, \mathcal{D}$ , and  $\mathcal{D}_c$  ▷  $VQ$  denotes a vector quantizer for VQ-reg.
while a maximum epoch is not reached do
  sample  $\mathbf{x}$  from  $\mathbf{X}$  ▷  $\mathbf{X}$  denotes a training dataset. In practice, a batch of  $\mathbf{x}$  is sampled.
   $\mathbf{x}_c \leftarrow$  stochastically extracting conditional well data from  $\mathbf{x}$ 

   $\mathbf{z}, \mathbf{z}_c \leftarrow \mathcal{E}(\mathbf{x}), \mathcal{E}_c(\mathbf{x}_c)$ 
   $\mathbf{z}_q, \ell_{VQ} = VQ(\mathbf{z})$  ▷  $\ell_{VQ}$  denotes a loss from VQ to reduce a gap between  $\mathbf{z}$  and  $\mathbf{z}_q$  (Van Den Oord et al., 2017).
   $(\mathbf{z}_q)_c, \ell_{VQ_c} = VQ_c(\mathbf{z}_c)$ 
   $\tilde{\mathbf{x}}, \tilde{\mathbf{x}}_c \leftarrow \text{softmax}(\mathcal{D}(\mathbf{z}_q)), \text{softmax}(\mathcal{D}_c((\mathbf{z}_q)_c))$ 

   $L_{\text{stage1}} \leftarrow \{CE(\mathbf{x}, \tilde{\mathbf{x}}) + CE(\mathbf{x}_c, \tilde{\mathbf{x}}_c)\} + \{\ell_{VQ} + \ell_{VQ_c}\}$ 

  update  $\mathcal{E}, \mathcal{E}_c, VQ, VQ_c, \mathcal{D}$ , and  $\mathcal{D}_c$  by minimizing  $L_{\text{stage1}}$ 
end while

```

Algorithm 2 Pseudocode of the training process of the proposed diffusion model (stage 2)

```

load the pretrained  $\mathcal{E}, \mathcal{E}_c, VQ, VQ_c, \mathcal{D}$ , and  $\mathcal{D}_c$ 
freeze  $\mathcal{E}$  and  $\mathcal{E}_c$ , while  $VQ, VQ_c, \mathcal{D}$ , and  $\mathcal{D}_c$  remain unfrozen
randomly initialize  $g_\theta$  and  $g_\phi$ 
while a maximum epoch is not reached do
  sample  $\mathbf{x}$  from  $\mathbf{X}$ 
   $\mathbf{x}_c \leftarrow$  stochastically extracting conditional well data from  $\mathbf{x}$ 

   $\mathbf{z}, \mathbf{z}_c \leftarrow \mathcal{E}(\mathbf{x}), \mathcal{E}_c(\mathbf{x}_c)$  ▷  $\mathbf{z} = \mathbf{z}_0$ 
   $\mathbf{z}_t \leftarrow$  forward diffusion process applied to  $\mathbf{z}_0$  ▷ adding noise to  $\mathbf{z}_0$ 
  if  $r \leq p_{\text{uncond}}$  then ▷  $r \sim U(0, 1)$  where  $U$  denotes a uniform distribution
     $\hat{\mathbf{z}}_0 \leftarrow g_\theta(\mathbf{z}_t, t)$  ▷ unconditional generation
     $L_{\text{LDM}} \leftarrow \|\mathbf{z}_0 - \hat{\mathbf{z}}_0\|_2^2$ 
     $\ell_{\text{LDM}} \leftarrow L_{\text{LDM}}$ 
  else
     $\hat{\mathbf{z}}_0 \leftarrow g_\theta(\mathbf{z}_t, t, g_\phi(\mathbf{z}_c))$  ▷ conditional generation
     $L_{\text{LDM},c} \leftarrow \|\mathbf{z}_0 - \hat{\mathbf{z}}_0\|_2^2$ 
     $\ell_{\text{LDM},c} \leftarrow L_{\text{LDM},c}$ 
  end if

   $\hat{\mathbf{z}}_q \leftarrow VQ(\hat{\mathbf{z}})$  ▷  $\hat{\mathbf{z}} = \hat{\mathbf{z}}_0$ 
   $\hat{\mathbf{x}} = \text{softmax}(\mathcal{D}(\hat{\mathbf{z}}_q))$ 
   $\hat{\mathbf{x}}_c \leftarrow$  retrieving the valid pixel locations in  $\mathbf{x}_c$  from  $\hat{\mathbf{x}}$ 
   $L_{\text{preserv}} \leftarrow CE(\mathbf{x}_c, \hat{\mathbf{x}}_c)$ 

   $L_{\text{stage2}} \leftarrow \ell_{\text{LDM}} + L_{\text{preserv}}$ 

  update  $VQ, VQ_c, \mathcal{D}, \mathcal{D}_c, g_\theta$ , and  $g_\phi$  by minimizing  $L_{\text{stage2}}$ 
end while

```

E Additional Experimental Results

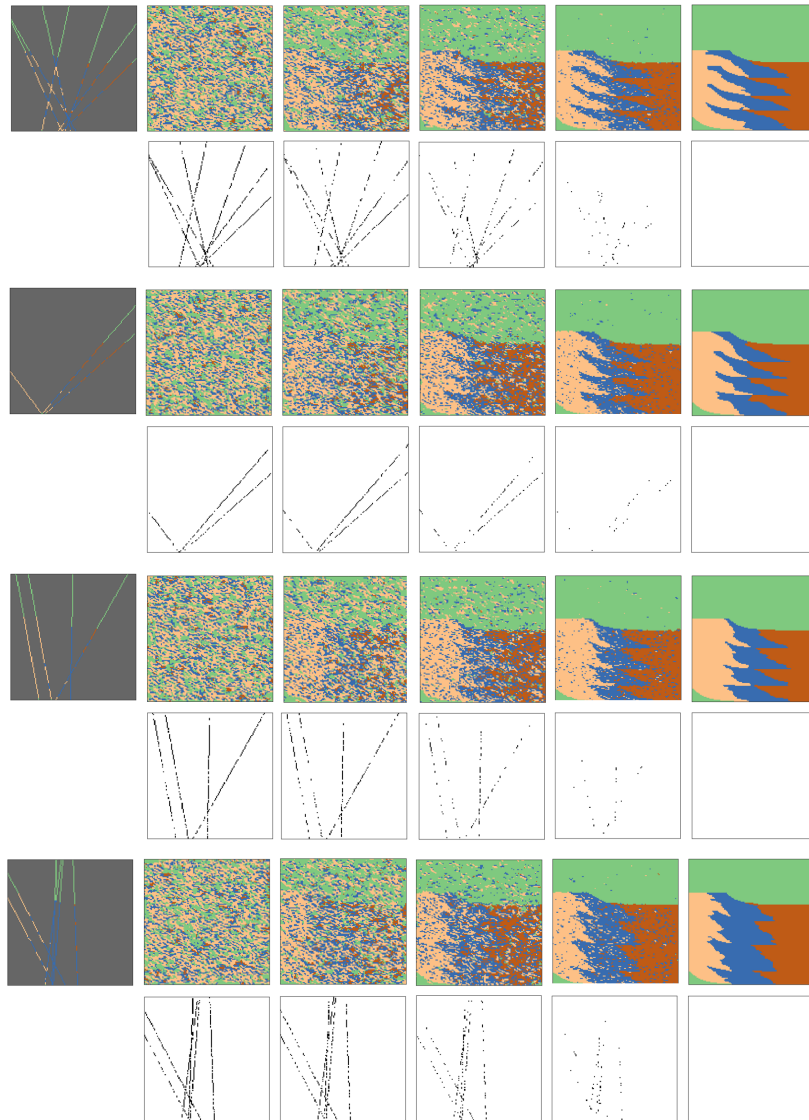


Figure 14: (continuation of Fig. 7) Additional examples of the transitions in the conditional denoising process.